




Article

In Situ XRD Measurement for High-Pressure Iron in Laser-Driven Off-Hugoniot State

Liang Sun ^{1,*}, Hao Liu ^{1,2}, Xiaoxi Duan ¹, Huan Zhang ¹, Zanyang Guan ¹, Weimin Yang ¹, Xiaokang Feng ³, Youjun Zhang ⁴ , Yulong Li ¹, Sanwei Li ¹, Dong Yang ¹, Zhebin Wang ¹, Jiamin Yang ¹, Jin Liu ⁵, Wenge Yang ³ , Toshimori Sekine ^{3,6,7}  and Zongqing Zhao ¹

¹ National Key Laboratory of Plasma Physics, Laser Fusion Research Center, Chinese Academy of Engineering Physics, Mianyang 621900, China

² Institute of Applied Physics and Computational Mathematics, Beijing 100094, China

³ Center for High Pressure Science and Technology Advanced Research (HPSTAR), Beijing 201203, China; yangwg@hpstar.ac.cn (W.Y.)

⁴ Institute of Atomic and Molecular Physics, Sichuan University, Chengdu 610065, China

⁵ Center for High Pressure Science (CHiPS), State Key Laboratory of Metastable Materials Science and Technology, Yanshan University, Qinhuangdao 066004, China

⁶ Graduate School of Engineering, Osaka University, Sakai 599-8531, Japan

⁷ Shanghai Key Laboratory of Material Frontiers Research in Extreme Environments (MFree), Shanghai 201203, China

* Correspondence: sunliangyp@outlook.com

Abstract: The investigation of iron under high pressure and temperatures is crucial to understand the Earth's core structure and composition and the generation of magnetic fields. Here, we present new in situ XRD measurements for iron in an off-Hugoniot state by laser-driven ramp compression at pressure of 200–238 GPa. The lattice parameters for the hexagonal (hcp)-Fe phase and the c/a ratios were obtained to compare them with previous static and dynamical data, which provides the direct confirmation of such parameters via the different compression paths and strain rates. This work indicates that laser ramp compression can be utilized to provide crystal structure information and direct key information on the crystal structure of Fe at the ultrahigh pressure–temperature conditions relevant for planetology.

Keywords: iron; high pressure; diffraction; lattice constant c/a ratio



Citation: Sun, L.; Liu, H.; Duan, X.; Zhang, H.; Guan, Z.; Yang, W.; Feng, X.; Zhang, Y.; Li, Y.; Li, S.; et al. In Situ XRD Measurement for High-Pressure Iron in Laser-Driven Off-Hugoniot State. *Minerals* **2024**, *14*, 715. <https://doi.org/10.3390/min14070715>

Academic Editor: Anna Pakhomova

Received: 27 May 2024

Revised: 5 July 2024

Accepted: 9 July 2024

Published: 15 July 2024



Copyright: © 2024 by the authors. Licensee MDPI, Basel, Switzerland. This article is an open access article distributed under the terms and conditions of the Creative Commons Attribution (CC BY) license (<https://creativecommons.org/licenses/by/4.0/>).

1. Introduction

As the main constituent of the interior of the Earth, the phase diagram of iron under high pressure (P) and temperature (T) conditions is crucial in comprehending the solid inner core and molten outer core [1–3]. Accurate knowledge of the crystal structure of iron (Fe) at the corresponding conditions is a vital piece of information for the elucidation of the seismological constraints of the Earth's inner core [4–7]. For instance, the non-ideal c/a ratio in the hcp structure could be linked to elastic anisotropy, and incorrect assessment would lead to erroneous conclusions concerning the seismological anisotropy exhibited by the Earth's inner core [7–9].

Iron at high pressure has been extensively investigated by static compression [2,10–12]. Above ~15 GPa, iron undergoes a transformation into the hexagonal close-packed phase (hcp-Fe) from the body-centered cubic (bcc-Fe) structure at ambient conditions. The hcp-Fe phase remains stable up to the maximum pressure of 354 GPa at 298 K [11]. However, only a limited number of experimental data have been reported beyond 200 GPa at high temperatures [13–16], where ab initio calculations have predicted the existence of bcc-Fe [4,5]. Previous studies have demonstrated that the c/a axial ratio of hcp-Fe increases substantially with increasing temperatures, indicating that the temperature has a significant influence on its elastic anisotropy [8,15,17]. The majority of the reported c/a ratios cluster

around 1.61 [18]. The c/a ratios for iron as a function of pressure have been reported to be around 1.61 (close to the ideal hcp value of 1.63), including the upper and lower limits of 1.67 and 1.59, respectively [17,18].

Dynamic compression provides an alternative approach for the investigation of the crystal structure in a wide range of pressure–temperature (P-T) conditions corresponding to the interiors of exoplanets and super-Earths [19–21]. Laser-driven shock compression has directly confirmed the hcp structure at low pressure through in situ X-ray diffraction (XRD) measurements in high-power laser facilities and XFEL [22–26]. The hcp phase of iron and its alloys has also been indicated experimentally at high stress [27–29]. Additionally, iron has been observed to undergo melting along the Hugoniot path at pressure of 230 to 270 GPa [30]. In dynamical experiments and simulations on single-crystal iron, a c/a ratio of ~ 1.7 has been observed [24,31]. These large c/a values can be explained by the lack of plasticity observed in shock compression within the limited timescale, leaving the interplanar spacing of the (011) plane orthogonal to the shock-loading direction. In contrast, the near-ideal c/a ratio of 1.61 for polycrystalline iron was found in laser shock experiments [24]. The current discrepancies observed between these dynamical and static studies of iron above 100 GPa have been attributed to non-equilibrium processes, casting doubt on the possibility of properly probing the phase diagrams of geophysically relevant materials using dynamic compression [22,32]. Furthermore, the kinetic features at the timescales of these experiments are quite different from those in static experiments [25].

Quasi-isentropic ramp compression is a well-controlled dynamical technique that allows materials to be compressed as the solid phase even at ultrahigh pressure by drastically reducing the temperature increase compared to shock compression [21,33,34]. The wide off-Hugoniot P-T conditions relevant to planetary interiors can be accessed by laser-driven shock-ramp compression, where the final temperature can also be controlled by the first Hugoniot temperature.

We provide new experimental data addressing these questions by probing iron at nanosecond timescales using in situ X-ray diffraction (XRD) measurements during the laser-driven ramp compression of Fe, offering the direct identification of the structure at the off-Hugoniot phase state. These X-ray diffraction results confirm the hcp-Fe under ramp compression at 200 GPa to 238 GPa. These pressure values are selected because there are sufficient data available in previous studies and because they are within the range of the Earth's core pressure. The structure parameters and the c/a ratios agree well with the static compression results. Furthermore, it is demonstrated that ramp compression on the nanosecond timescale is suitable for the study of iron under conditions relevant to the deep interiors of planets, which is difficult to achieve with static compression techniques. This approach could provide direct key information on the crystal structure of Fe at the ultrahigh pressure–temperature conditions relevant for planetology.

2. Materials and Methods

The dynamical experiments to probe the structure change of iron at high pressure were conducted at the 100-kJ-level laser facility in the Laser Fusion Research Center (LFRC) [35–37]. This laser facility is capable of operating at an ultraviolet wavelength of 351 nm with multiple beams. The in situ X-ray powder diffraction (XRD) experimental technique, coupled with laser-driven dynamical compression at the LFRC, has been developed in recent years [38,39]. This technique enables the determination of the crystal structure of matter under extreme conditions. Figure 1 provides the details of the experimental configurations employed in the present study.

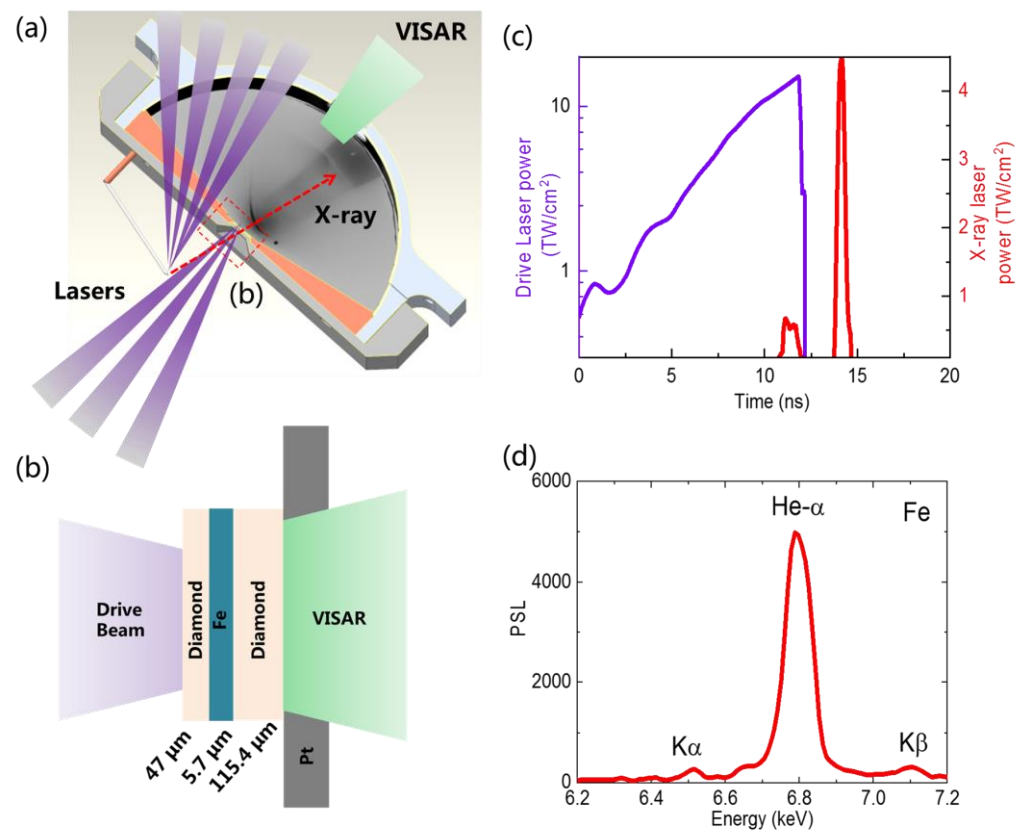


Figure 1. Experimental setup, target configuration and laser profiles in laser ramp compression experiments. (a) Dynamical compression with in situ X-ray diffraction measurement was created by nanosecond lasers. Several beams irradiated the Fe foil to generate the monochromatic X-ray flash for XRD measurement. The XRD snapshot was documented by image plates in the steel diagnostic box when a series of laser pulses drove the sample in the center of box to achieve an extremely high-pressure state. (b) Dynamical compression for the diamond–Fe–diamond layer target with a specific thickness was generated by drive laser beams. A line-imaging velocimetry (VISAR) device monitored the diamond window to reconstruct the off-Hugoniot pressure history of iron under dynamical compression. (c) Laser profile in shot 092. The main driven laser for the sample was the ~ 12 ns pulse shape (purple curve) with a gradually increasing intensity as ramp compression. A 500 ps square pulse with a 1-nanosecond initial pre-pulse (red curve) at the proper relative time was adopted to create X-ray source. (d) The detected Fe X-ray source emission in shot 092.

As illustrated in Figure 1a, the monochromatic X-ray flash for XRD measurement during laser-driven dynamical compression was created and time-controlled by multi-nanosecond laser beams. The X-ray flash was emitted at an angle of 20° with respect to the normal of the main target. The XRD snapshot was recorded by image plates inside the developed steel diagnostic box when a series of laser pulses drove the sample at the center of the box to achieve an extremely high-pressure state. Figure 1b shows the details of the laser-driven samples used in the experiment. Diamond–Fe–diamond planar sandwich samples were designed for the experiment. The surface of the first diamond was ablated by the increasing power of the laser drive beams, producing a series of pressure waves that propagated through the target package and ramp-compressed the Fe sample through multiple wave reverberations. The compression waves eventually reached the rear surface of the back diamond, accelerating it into free space. Velocimetry provided measurements of the free surface velocities, which were used to determine the stress state in the Fe sample. The sandwich target was mounted on a platinum plate with a 400- μm -diameter pinhole aperture. The 1000 μm laser-driven spot was large relative to the collimating aperture,

to limit the X-ray diffraction velocimetry diagnostic field of view to the center of the laser-compressed region of the sample.

An ultraviolet 351 nm laser pulse was shaped to produce an irradiance profile that smoothly increased the pressure in the sample. This ramped pulse was designed to avoid shock formation. A single beam with a 1000 μm focal spot drove the targets with 12 ns pluses and laser intensities that ramped up to $15 \times 10^{12} \text{ W/cm}^2$. The laser drive beams irradiated the Fe sandwich target at an angle of 25° with respect to the target normal. The additional laser beams irradiated the Fe foil with an irradiative value of $4.5 \times 10^{14} \text{ W/cm}^2$ per beam to optimize the laser energy to the X-ray efficiency. The typical delivered pulse shape is shown as a function of time in Figure 1c.

The X-ray source (XRS) was generated by laser-irradiating the Fe film target ($2 \times 2 \text{ mm}^2$ square, 15 μm thick) over the duration of the laser pulse and emitted as a quasi-monochromatic 6.7-keV He- α X-ray. The dominant line spectrum emitted was measured with multiple crystal X-ray spectrometers and is displayed in Figure 1d. We used the Pt pinhole to collimate the X-rays and as a reference to precisely determine the diffraction geometry. As shown in Figure 1a, the Debye–Scherrer diffraction cones from both the compressed sample and ambient Pt were recorded on the image plates (IPs). We inserted Fe filters to suppress the helium-like β and γ X-rays, in addition to the Bremsstrahlung continuum X-ray emission from the drive plasma, which caused dominant noise to be recorded on the IPs. The 2θ and d spacing resolution for this diagnostic (1° and 2.5% in Fe X-ray sources) was calibrated by considering spectral broadening, a finite XRS size, and a finite pinhole diameter.

The iron (99% purity) samples were rolled foils with a limited preferred orientation (texture) of the crystal grains evident in the diffraction data. The Fe samples (5.7 μm thick) were sandwiched between a $\langle 100 \rangle$ orientated 47 μm single-crystal diamond ablator or pusher and a $\langle 100 \rangle$ orientated 120- μm -thick single-crystal diamond window.

A line-imaging velocity interferometer system for any reflector (VISAR) [40,41] detects the Doppler shifts of a 532 nm probe beam reflecting off the rear side of the diamond window. The fringe pattern shifts recorded in a 2D interferogram display the Doppler shifts and are proportional to the changes in the velocity of the reflecting surface. The velocity for the rear surface of the diamond window as a function of time will determine the pressure history of the Fe sample, which was used to infer the sample pressure at the X-ray snapshot. As seen in Figure 1a, the in situ diffraction box allows the VISAR probe to reflect off the rear surface of the target mounted on the front of box. The pressure determination from the measured free surface velocities and the results of the X-ray diffraction analysis will be discussed in the next section.

3. Results

The XRD image of the compressed sample was collected in the diagnostic box. After identifying the direct X-ray source and the diffraction calibration signals from the ambient Pt reference, the data were projected into the $2\theta - \varnothing$ space, where \varnothing is the azimuthal angle around the Debye–Scherrer ring. We performed a least-squares minimization routine to determine the best-fit values for the experimental geometry, including the image plate, XRS, and pinhole locations. Figure 2 illustrates the azimuthally averaged lineouts of the 2θ projections of the X-ray diffraction pattern, which were measured in two shots. It shows the three diffraction lines in (100), (101), and (002) reflection and the ambient Pt XRD peaks. The diffraction peaks of iron indicate the hcp structure of Fe. Neither diffraction peaks from the bcc-Fe phase nor those from the fcc-Fe phase were found in the shots. The Bragg condition was used to calculate the d spacings from the measured diffraction angle 2θ . The lattice parameters a and c were calculated from the three d values to obtain the c/a ratios.

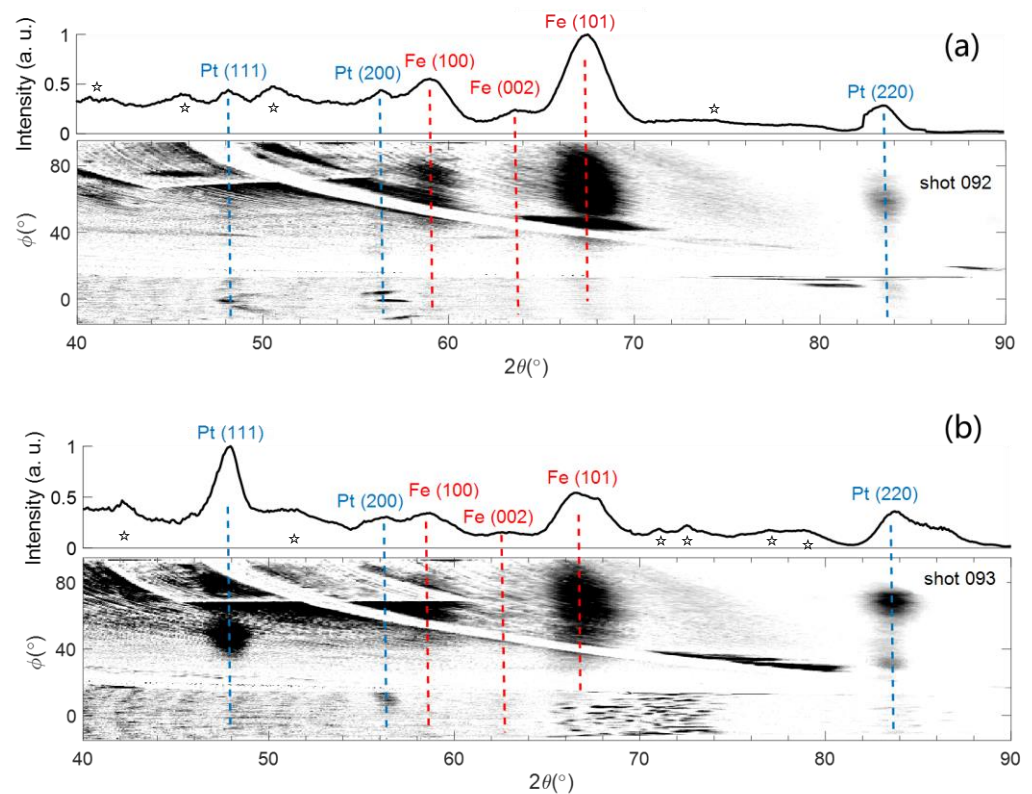


Figure 2. The X-ray diffraction patterns of iron observed in shot 092 (a) and shot 093 (b). The diffraction patterns were projected into the $2\theta - \phi$ plane after subtracting the background. The blue dashed lines show the peak positions of the reference Pt at ambient conditions for calibration. The red dashed lines show the peaks from compressed Fe as indexed $(h\ l\ k)$ for hcp-Fe. The peaks marked by stars (\star) are ghosts from IP faults and background noise.

The accurate pressure measurements in the shots were facilitated with the use of single-crystal diamond windows by obtaining the rear side velocities using VISAR [38,39,42]. Diamond windows become opaque under shock or ramp compression when the pressure is above the diamond elastic limit (HEL) [42–44]. To determine the mean pressure within the finite-thickness Fe sample, a correction was applied to the C-Fe-C pressure using the measured free surface velocity. Taking into account the laser profile in Figure 3a in shot 092, the free surface velocity of diamond, outlined in Figure 3b, was measured after about 11 ns with accuracy of 5% of the velocity per fringe (VPF). The VPFs used in the two interferometers were 7.12 and 2.78 $\mu\text{m}/\text{ns}$ fringe.

The characteristic algorithm was used to map the pressure in the Fe sample in space and time [45–47], as shown in Figure 3c. The inputs into the characteristic propagation algorithm include the measured rear-surface diamond particle velocity, the EOS for diamond [48], the sample thickness, and the XRS probe time and duration.

Figure 3d shows the whole procedure of determining the pressure parameter of iron at the X-ray diffraction time. The average pressure throughout the thickness of the Fe over the duration of the X-ray probe was determined, as shown in Figure 3c,d. The uncertainty for the pressure mainly comes from the free surface velocities in VISAR. To assess the errors, the characteristic calculation was performed by varying the velocity histories within their uncertainties. The mean and standard deviation were given as the value and error for the measured pressure during the X-ray exposure. The standard deviation of the mean pressure state in the sample was estimated to be $\sim 4\%$ relative to the mean pressure. However, due to the failure of the uniform-planar VISAR records in shot 093, it was difficult to determine the pressure using the characteristic algorithm method. Considering experimental conditions similar to those of shot 092, the pressure of ~ 200 GPa was estimated from the known isentropic EOS data [33] and the density measured in the XRD data. Therefore, two in situ

XRD results on hcp-Fe under ramp compression were obtained to calculate the c/a ratio at the off-Hugoniot state at pressure of ~ 200 GPa to $238 (\pm 7)$ GPa.

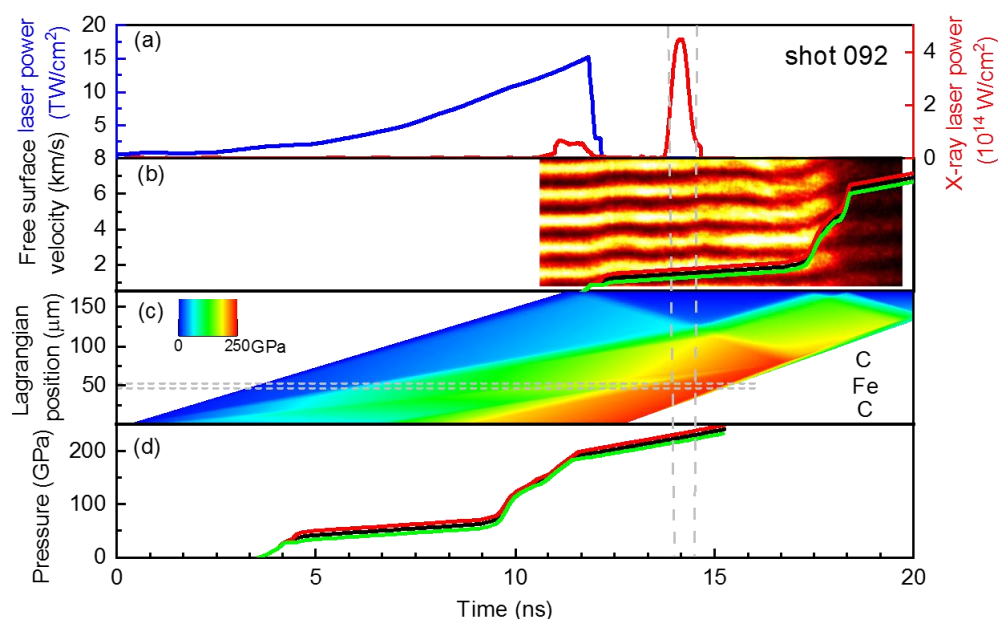


Figure 3. The constructed compression state for iron at high pressure in shot 092. (a) The laser pulses indicate that the X-ray diffraction recording time at ~ 14 ns was near the time for peak compression. (b) The VISAR data recorded the extracted free surfaces of diamond windows with experimental uncertainties (red, black, green curves). The velocity history shows that the first velocity jump at ~ 1.5 km/s is followed by ramp loading in ~ 5 ns to peak compression velocity ~ 7.5 km/s, and the single-crystal diamond becomes opaque under ramp compression. (c) The constructed stress map in the C-Fe-C target as a function of time by characteristic calculation. The horizontal dashed lines show the boundaries of the diamond ablator, iron sample, and diamond window in the target. The vertical dashed lines show the ~ 0.5 ns time duration in X-ray diffraction measurement. (d) The averaged stress for the iron sample as a function of time. In this shot, the deduced pressure for iron at the XRD time is 238 GPa.

4. Discussion

The crystal structures of hcp metals are often characterized by the ratio of the lattice parameters, c/a , as a function of the pressure or volume to provide insights into the atomic packing and extreme deformation mechanisms of such metals. Tracking the c/a ratio could provide insights into the underlying physical and/or process parameters (e.g., static vs. dynamic compression, including the strain rate) that dictate the deformation response in impacted materials, including the typical timescales of the phase transformation of materials exposed to extreme conditions. For the present study, Table 1 lists the detailed experimental results regarding the observed d values and calculated c/a ratios.

Table 1. The experimental results for solid iron under ramp compression. The d values for each reflection and the axial c/a ratio of the hcp structure were measured.

Shot No.	Stress (GPa)	d (100) Å	d (002) Å	d (101) Å	Density	c/a Ratio
092	238 (7)	1.88 (2)	1.74 (4)	1.66 (1)	13.1 (4)	1.604 (38)
093	200 ¹	1.90 (2)	1.77 (4)	1.66 (1)	12.6 (4)	1.616 (40)

¹ The pressure was estimated from the measured density with the equation of state data in Ref. [33].

Figure 4 compares the c/a ratios between iron and the iron alloy containing 7% by weight of silicon (Fe-7wt%Si) at high pressure, indicating that the Si-bearing alloy has a

slightly higher value than pure iron. The presence of silicon in the Fe-Si alloy (with 7 wt% Si) has the effect of increasing the c/a ratio, as evidenced when comparing our data with the shock data reported in Refs. [27,49]. The experimental results from static compression show that the temperature dependence of the c/a ratio is very weak up to 350 GPa, although it depends upon the pressure scale above 200 GPa [50]. In comparison with previous shock compression results, our dynamic ramp compression data at pressure of ~200 GPa to ~240 GPa are closer to the static results indicating a c/a ratio of approximately 1.60. The difference between the dynamic and static results may be explained by the temperature effect.

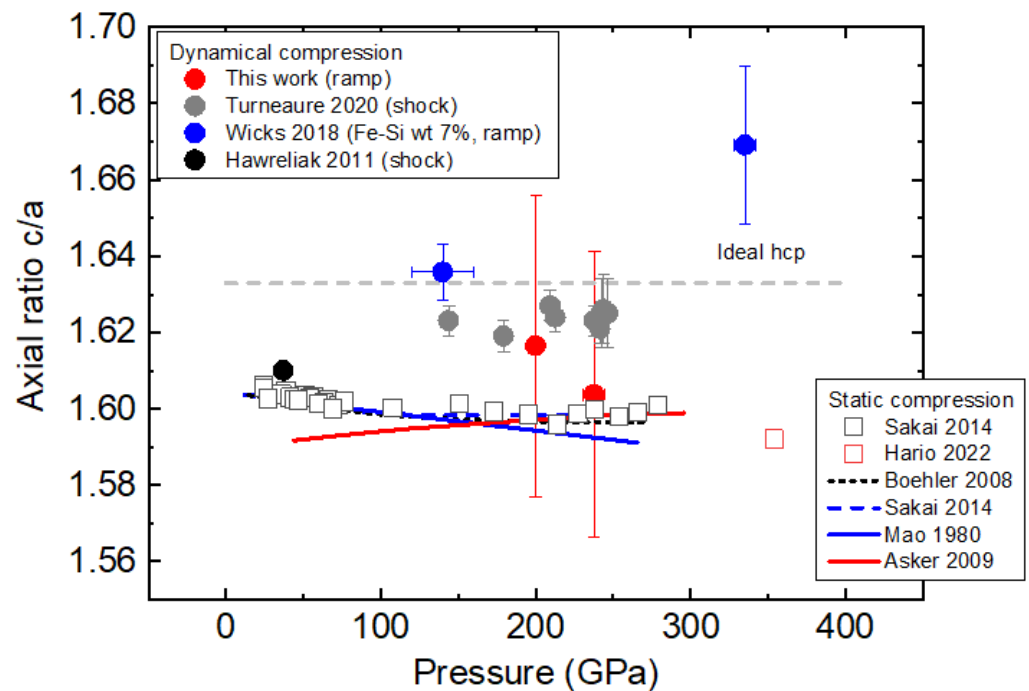


Figure 4. The c/a ratio of hcp-iron at high pressure by static and dynamical compression. The ideal c/a ratio for the hcp structure (grey dashed line) and the typical measurement data (black and red squares) with fitting data in Ref. [18] (black dotted, blue dashed, red, blue lines) are plotted for comparison. The ratios from the previous dynamical compression (black, grey, blue circles) from Refs. [24,27,49] are illustrated. Our ramp compression data are between those of previous shock experiments and the static compression data.

In principle, the temperature rise in shock compression is higher than that in shockless or ramp compression. Along the Hugoniot path, the shock temperature at pressure of ~240 GPa was measured as ~6000 K (Refs. [30,51]). The stability of the hcp structure along the Hugoniot is achieved through shock melting, which occurs between ~242 and ~247 GPa. The melting temperature is estimated to be 5100 K at 200 GPa [30]. Furthermore, the hcp-iron c/a ratios are nearly independent of the shock stress, with values ranging from 1.619 to 1.627 at pressure of ~150–250 GPa.

Compared with shock compression, ramp compression at the nanosecond timescale is suitable for the study of iron under conditions relevant to the deep interiors of planets. Figure 5 shows the relationship between the volume and c/a ratio for iron and iron alloy at high pressure. In the same pressure region, the c/a ratio and compressed volume for iron in our measurement are slightly lower than those in the previous shock data in Ref. [49], but close to those obtained in static compression. The discrepancies observed in the previous dynamical and static studies of iron above 100 GPa in Refs. [22,32] may be caused by the temperature effect or kinetic features on the timescale of dynamical compression [25], although the static pressure is affected by the pressure calibration method.

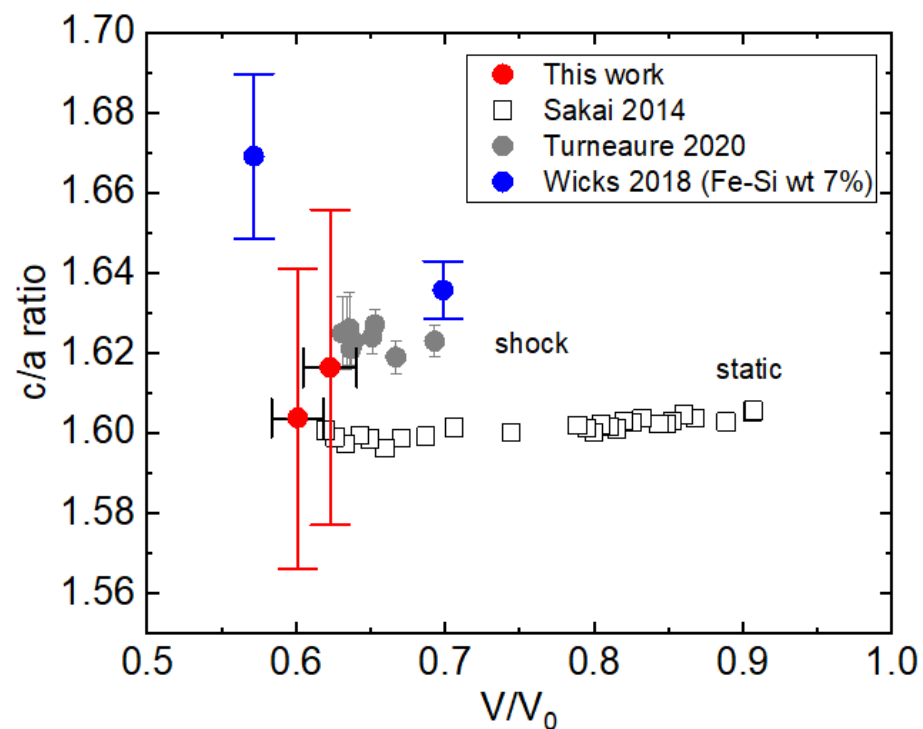


Figure 5. The volume- c/a ratio relationship for iron and iron alloy at high pressure. The c/a ratios in static compression (squares) from Ref. [18] and in the previous dynamical compression (grey, blue circles) from Refs. [27,49] are illustrated for comparison. Our data obtained in ramp-compressed iron are illustrated in red circles. The initial volume used for V/V_0 calculation in static compression from Ref. [18] is 22.468 \AA^3 .

In this work, the free velocity history confirms the nearly isentropic ramp compression from the initial compressed state. The initial compression at pressure of ~ 50 GPa is expected to be due to a temperature rise of ~ 1000 K [49]. Then, the ramp compression will increase the temperature slightly due to the isentropic compression and plastic work heating. The exact temperature estimate for iron requires knowledge of the plastic work heating in diamond [48,52,53], thermal conductance in diamond and iron, and plastic heating in iron. Based on the volume change, the temperature during ramp compression is significantly lower than that in shock compression at a given pressure level. The development of an extended X-ray absorption fine structure (EXAFS) in a laser facility could allow us to directly measure the temperature profiles for iron at the relevant off-Hugoniot state in the near future [29,54].

5. Conclusions

In conclusion, we conducted two dynamical experiments to probe the structure of iron at high pressure in the 100-kJ-level laser facility. By combining in situ XRD diagnostic and VISAR measurement, the crystal structure for ramp-compressed Fe has been studied at pressure of ~ 200 GPa to ~ 240 GPa and three typical diffraction peaks of hcp-Fe have been detected in an off-Hugoniot P-T condition. The obtained d spacing, c/a ratio and compressed volume agree well with the previous static experiment results. By comparing them with the data in previous shock compression, the present c/a ratio and compressed volume for iron are slightly lower and indicate that the temperature during ramp compression is relatively cooler than that in shock compression. Our work also casts doubt on the possibility of properly probing the phase diagrams of relevant materials using laser ramp compression and indicates that laser ramp compression can be utilized to provide key crystal structure information on Fe at the ultrahigh pressure-temperature conditions relevant for planetology.

Author Contributions: Conceptualization, L.S.; methodology, H.L. and X.D.; software, H.Z.; validation, Y.Z. and X.F.; formal analysis, W.Y. (Weimin Yang); investigation, L.S., H.L. and Z.G.; resources, J.Y. and Z.Z.; data curation, J.L. and Y.L.; writing—original draft preparation, L.S.; writing—review and editing, W.Y. (Wenge Yang) and T.S.; visualization, Z.W.; supervision, S.L. and D.Y.; project administration, Z.Z.; funding acquisition, H.L. and Z.W. All authors have read and agreed to the published version of the manuscript.

Funding: This research was funded by the National Natural Science Foundation of China, Grants No. 12205276 and No. 12035002.

Data Availability Statement: All experimental data in this work are available upon request.

Acknowledgments: We acknowledge the crucial contributions of the 100-kJ-level laser management, staff, and support team to the shots. We thank the target support team for preparing the target.

Conflicts of Interest: The authors declare no conflicts of interest. The funders had no role in the design of the study; in the collection, analyses, or interpretation of the data; in the writing of the manuscript; or in the decision to publish the results.

References

1. Mao, H.; Mao, W.L. Key Problems of the Four-Dimensional Earth System. *Matter Radiat. Extrem.* **2020**, *5*, 038102. [[CrossRef](#)]
2. Mao, H.-K.; Chen, B.; Gou, H.; Li, K.; Liu, J.; Wang, L.; Xiao, H.; Yang, W. 2022 HP Special Volume: Interdisciplinary High Pressure Science and Technology. *Matter Radiat. Extrem.* **2023**, *8*, 063001. [[CrossRef](#)]
3. Birch, F. Elasticity and Constitution of the Earth's Interior. *J. Geophys. Res.* **1952**, *57*, 227–286. [[CrossRef](#)]
4. Belonoshko, A.B.; Lukinov, T.; Fu, J.; Zhao, J.; Davis, S.; Simak, S.I. Stabilization of Body-Centred Cubic Iron under Inner-Core Conditions. *Nat. Geosci.* **2017**, *10*, 312–316. [[CrossRef](#)]
5. Belonoshko, A.B.; Ahuja, R.; Johansson, B. Stability of the Body-Centred-Cubic Phase of Iron in the Earth's Inner Core. *Nature* **2003**, *424*, 1032–1034. [[CrossRef](#)] [[PubMed](#)]
6. Sun, Y.; Zhang, F.; Mendelev, M.I.; Wentzcovitch, R.M.; Ho, K.-M. Two-Step Nucleation of the Earth's Inner Core. *Proc. Natl. Acad. Sci. USA* **2022**, *119*, e2113059119. [[CrossRef](#)] [[PubMed](#)]
7. Sun, S.; He, Y.; Yang, J.; Lin, Y.; Li, J.; Kim, D.Y.; Li, H.; Mao, H. Superionic Effect and Anisotropic Texture in Earth's Inner Core Driven by Geomagnetic Field. *Nat. Commun.* **2023**, *14*, 1656. [[CrossRef](#)]
8. Steinle-Neumann, G.; Stixrude, L.; Cohen, R.E.; Gülseren, O. Elasticity of Iron at the Temperature of the Earth's Inner Core. *Nature* **2001**, *413*, 57–60. [[CrossRef](#)]
9. He, Y.; Sun, S.; Kim, D.Y.; Jang, B.G.; Li, H.; Mao, H. Superionic Iron Alloys and Their Seismic Velocities in Earth's Inner Core. *Nature* **2022**, *602*, 258–262. [[CrossRef](#)]
10. Mao, H.-K.; Chen, X.-J.; Ding, Y.; Li, B.; Wang, L. Solids, Liquids, and Gases under High Pressure. *Rev. Mod. Phys.* **2018**, *90*, 015007. [[CrossRef](#)]
11. Hirao, N.; Akahama, Y.; Ohishi, Y. Equations of State of Iron and Nickel to the Pressure at the Center of the Earth. *Matter Radiat. Extrem.* **2022**, *7*, 038403. [[CrossRef](#)]
12. Zeng, Q. In Situ High-Pressure Wide-Angle Hard x-Ray Photon Correlation Spectroscopy: A Versatile Tool Probing Atomic Dynamics of Extreme Condition Matter. *Matter Radiat. Extrem.* **2023**, *8*, 028101. [[CrossRef](#)]
13. Dorogokupets, P.I.; Dymshits, A.M.; Litasov, K.D.; Sokolova, T.S. Thermodynamics and Equations of State of Iron to 350 GPa and 6000 K. *Sci. Rep.* **2017**, *7*, 41863. [[CrossRef](#)]
14. Tateno, S.; Hirose, K.; Ohishi, Y.; Tatsumi, Y. The Structure of Iron in Earth's Inner Core. *Science* **2010**, *330*, 359–361. [[CrossRef](#)]
15. Anzellini, S.; Dewaele, A.; Mezouar, M.; Loubeyre, P.; Morard, G. Melting of Iron at Earth's Inner Core Boundary Based on Fast X-ray Diffraction. *Science* **2013**, *340*, 464–466. [[CrossRef](#)]
16. Sinmyo, R.; Hirose, K.; Ohishi, Y. Melting Curve of Iron to 290 GPa Determined in a Resistance-Heated Diamond-Anvil Cell. *Earth Planet. Sci. Lett.* **2019**, *510*, 45–52. [[CrossRef](#)]
17. Dewaele, A.; Loubeyre, P.; Occelli, F.; Mezouar, M.; Dorogokupets, P.I.; Torrent, M. Quasihydrostatic Equation of State of Iron above 2 Mbar. *Phys. Rev. Lett.* **2006**, *97*, 215504. [[CrossRef](#)]
18. Sakai, T.; Takahashi, S.; Nishitani, N.; Mashino, I.; Ohtani, E.; Hirao, N. Equation of State of Pure Iron and Fe_{0.9}Ni_{0.1} Alloy up to 3Mbar. *Phys. Earth Planet. Inter.* **2014**, *228*, 114–126. [[CrossRef](#)]
19. Duffy, T.S. Mineralogy at the Extremes. *Nature* **2008**, *451*, 269–270. [[CrossRef](#)] [[PubMed](#)]
20. Fei, Y.; Seagle, C.T.; Townsend, J.P.; McCoy, C.A.; Boujibar, A.; Driscoll, P.; Shulenburg, L.; Furnish, M.D. Melting and Density of MgSiO₃ Determined by Shock Compression of Bridgmanite to 1254 GPa. *Nat. Commun.* **2021**, *12*, 876. [[CrossRef](#)] [[PubMed](#)]
21. Duffy, T.S.; Smith, R.F. Ultra-High Pressure Dynamic Compression of Geological Materials. *Front. Earth Sci.* **2019**, *7*, 23. [[CrossRef](#)]
22. Tecklenburg, S.; Colina-Ruiz, R.; Hok, S.; Bolme, C.; Galtier, E.; Granados, E.; Hashim, A.; Lee, H.J.; Merkel, S.; Morrow, B.; et al. Ultrafast X-ray Diffraction Study of a Shock-Compressed Iron Meteorite above 100 GPa. *Minerals* **2021**, *11*, 567. [[CrossRef](#)]

23. Kalantar, D.H.; Belak, J.F.; Collins, G.W.; Colvin, J.D.; Davies, H.M.; Eggert, J.H.; Germann, T.C.; Hawreliak, J.; Holian, B.L.; Kadau, K.; et al. Direct Observation of the $\alpha - \epsilon$ Transition in Shock-Compressed Iron via Nanosecond X-ray Diffraction. *Phys. Rev. Lett.* **2005**, *95*, 075502. [[CrossRef](#)]
24. Hawreliak, J.A.; El-Dasher, B.; Lorenzana, H.; Kimminau, G.; Higginbotham, A.; Nagler, B.; Vinko, S.M.; Murphy, W.J.; Whitcher, T.; Wark, J.S.; et al. In Situ X-ray Diffraction Measurements of the c / a Ratio in the High-Pressure ϵ Phase of Shock-Compressed Polycrystalline Iron. *Phys. Rev. B* **2011**, *83*, 144114. [[CrossRef](#)]
25. Hwang, H.; Galtier, E.; Cynn, H.; Eom, I.; Chun, S.H.; Bang, Y.; Hwang, G.C.; Choi, J.; Kim, T.; Kong, M.; et al. Subnanosecond Phase Transition Dynamics in Laser-Shocked Iron. *Sci. Adv.* **2020**, *6*, eaaz5132. [[CrossRef](#)]
26. Denoeud, A.; Ozaki, N.; Benuzzi-Mounaix, A.; Uranishi, H.; Kondo, Y.; Kodama, R.; Brambrink, E.; Ravasio, A.; Bocoum, M.; Boudenne, J.-M.; et al. Dynamic X-ray Diffraction Observation of Shocked Solid Iron up to 170 GPa. *Proc. Natl. Acad. Sci. USA* **2016**, *113*, 7745–7749. [[CrossRef](#)]
27. Wicks, J.K.; Smith, R.F.; Fratanduono, D.E.; Coppari, F.; Kraus, R.G.; Newman, M.G.; Rygg, J.R.; Eggert, J.H.; Duffy, T.S. Crystal Structure and Equation of State of Fe-Si Alloys at Super-Earth Core Conditions. *Sci. Adv.* **2018**, *4*, eaao5864. [[CrossRef](#)]
28. Kraus, R.G.; Hemley, R.J.; Ali, S.J.; Belof, J.L.; Benedict, L.X.; Bernier, J.; Braun, D.; Cohen, R.E.; Collins, G.W.; Coppari, F.; et al. Measuring the Melting Curve of Iron at Super-Earth Core Conditions. *Science* **2022**, *375*, 202–205. [[CrossRef](#)]
29. Ping, Y.; Coppari, F.; Hicks, D.G.; Yaakobi, B.; Fratanduono, D.E.; Hamel, S.; Eggert, J.H.; Rygg, J.R.; Smith, R.F.; Swift, D.C.; et al. Solid Iron Compressed Up to 560 GPa. *Phys. Rev. Lett.* **2013**, *111*, 065501. [[CrossRef](#)] [[PubMed](#)]
30. Li, J.; Wu, Q.; Li, J.; Xue, T.; Tan, Y.; Zhou, X.; Zhang, Y.; Xiong, Z.; Gao, Z.; Sekine, T. Shock Melting Curve of Iron: A Consensus on the Temperature at the Earth's Inner Core Boundary. *Geophys. Res. Lett.* **2020**, *47*, e2020GL087758. [[CrossRef](#)]
31. Hawreliak, J.; Colvin, J.D.; Eggert, J.H.; Kalantar, D.H.; Lorenzana, H.E.; Stölken, J.S.; Davies, H.M.; Germann, T.C.; Holian, B.L.; Kadau, K.; et al. Analysis of the X-ray Diffraction Signal for the $\alpha - \epsilon$ Transition in Shock-Compressed Iron: Simulation and Experiment. *Phys. Rev. B* **2006**, *74*, 184107. [[CrossRef](#)]
32. Merkel, S.; Hok, S.; Bolme, C.; Rittman, D.; Ramos, K.J.; Morrow, B.; Lee, H.J.; Nagler, B.; Galtier, E.; Granados, E.; et al. Femtosecond Visualization of Hcp-Iron Strength and Plasticity under Shock Compression. *Phys. Rev. Lett.* **2021**, *127*, 205501. [[CrossRef](#)]
33. Smith, R.F.; Fratanduono, D.E.; Braun, D.G.; Duffy, T.S.; Wicks, J.K.; Celliers, P.M.; Ali, S.J.; Fernandez-Pañella, A.; Kraus, R.G.; Swift, D.C.; et al. Equation of State of Iron under Core Conditions of Large Rocky Exoplanets. *Nat. Astron.* **2018**. [[CrossRef](#)]
34. Wang, J.; Smith, R.F.; Eggert, J.H.; Braun, D.G.; Boehly, T.R.; Reed Patterson, J.; Celliers, P.M.; Jeanloz, R.; Collins, G.W.; Duffy, T.S. Ramp Compression of Iron to 273 GPa. *J. Appl. Phys.* **2013**, *114*, 023513. [[CrossRef](#)]
35. Gong, T.; Hao, L.; Li, Z.; Yang, D.; Li, S.; Li, X.; Guo, L.; Zou, S.; Liu, Y.; Jiang, X.; et al. Recent Research Progress of Laser Plasma Interactions in Shenguang Laser Facilities. *Matter Radiat. Extrem.* **2019**, *4*, 055202. [[CrossRef](#)]
36. Wang, F.; Jiang, S.; Ding, Y.; Liu, S.; Yang, J.; Li, S.; Huang, T.; Cao, Z.; Yang, Z.; Hu, X.; et al. Recent Diagnostic Developments at the 100 kJ-Level Laser Facility in China. *Matter Radiat. Extrem.* **2020**, *5*, 035201. [[CrossRef](#)]
37. Sun, L.; Zhang, H.; Guan, Z.; Yang, W.; Zhang, Y.; Sekine, T.; Duan, X.; Wang, Z.; Yang, J. Sound Velocity Measurement of Shock-Compressed Quartz at Extreme Conditions. *Minerals* **2021**, *11*, 1334. [[CrossRef](#)]
38. Rygg, J.R.; Eggert, J.H.; Lazicki, A.E.; Coppari, F.; Hawreliak, J.A.; Hicks, D.G.; Smith, R.F.; Sorce, C.M.; Uphaus, T.M.; Yaakobi, B.; et al. Powder Diffraction from Solids in the Terapascal Regime. *Rev. Sci. Instrum.* **2012**, *83*, 113904. [[CrossRef](#)]
39. Rygg, J.R.; Smith, R.F.; Lazicki, A.E.; Braun, D.G.; Fratanduono, D.E.; Kraus, R.G.; McNaney, J.M.; Swift, D.C.; Wehrenberg, C.E.; Coppari, F.; et al. X-ray Diffraction at the National Ignition Facility. *Rev. Sci. Instrum.* **2020**, *91*, 043902. [[CrossRef](#)] [[PubMed](#)]
40. Celliers, P.M.; Bradley, D.K.; Collins, G.W.; Hicks, D.G.; Boehly, T.R.; Armstrong, W.J. Line-Imaging Velocimeter for Shock Diagnostics at the OMEGA Laser Facility. *Rev. Sci. Instrum.* **2004**, *75*, 4916–4929. [[CrossRef](#)]
41. Celliers, P.M.; Millot, M. Imaging Velocity Interferometer System for Any Reflector (VISAR) Diagnostics for High Energy Density Sciences. *Rev. Sci. Instrum.* **2023**, *94*, 011101. [[CrossRef](#)]
42. Lazicki, A.; Rygg, J.R.; Coppari, F.; Smith, R.; Fratanduono, D.; Kraus, R.G.; Collins, G.W.; Briggs, R.; Braun, D.G.; Swift, D.C.; et al. X-ray Diffraction of Solid Tin to 1.2 TPa. *Phys. Rev. Lett.* **2015**, *115*, 075502. [[CrossRef](#)]
43. McWilliams, R.S.; Eggert, J.H.; Hicks, D.G.; Bradley, D.K.; Celliers, P.M.; Spaulding, D.K.; Boehly, T.R.; Collins, G.W.; Jeanloz, R. Strength Effects in Diamond under Shock Compression from 0.1 to 1 TPa. *Phys. Rev. B* **2010**, *81*, 014111. [[CrossRef](#)]
44. Katagiri, K.; Ozaki, N.; Miyanishi, K.; Kamimura, N.; Umeda, Y.; Sano, T.; Sekine, T.; Kodama, R. Optical Properties of Shock-Compressed Diamond up to 550 GPa. *Phys. Rev. B* **2020**, *101*, 184106. [[CrossRef](#)]
45. Rothman, S.; Davis, J.-P.; Gooding, S.; Knudson, M.; Ao, T. Measurement of the Principal Quasi-Isentrope of Lead to ~3Mbar Using the “Z” Machine. *J. Phys. Conf. Ser.* **2014**, *500*, 032016. [[CrossRef](#)]
46. Ali, S.J.; Kraus, R.G.; Fratanduono, D.E.; Swift, D.C.; Eggert, J.H. An Iterative Forward Analysis Technique to Determine the Equation of State of Dynamically Compressed Materials. *J. Appl. Phys.* **2017**, *121*, 195901. [[CrossRef](#)]
47. Maw, J.R. A Characteristics Code for Analysis of Isentropic Compression Experiments. In Proceedings of the Conference of the American Physical Society Topical Group on Shock Compression of Condensed Matter, Portland, ON, USA, 20–25 July 2003; Volume 706, pp. 1217–1220.
48. Bradley, D.K.; Eggert, J.H.; Smith, R.F.; Prisbrey, S.T.; Hicks, D.G.; Braun, D.G.; Biener, J.; Hamza, A.V.; Rudd, R.E.; Collins, G.W. Diamond at 800 GPa. *Phys. Rev. Lett.* **2009**, *102*. [[CrossRef](#)]

49. Turneure, S.J.; Sharma, S.M.; Gupta, Y.M. Crystal Structure and Melting of Fe Shock Compressed to 273 GPa: In Situ X-ray Diffraction. *Phys. Rev. Lett.* **2020**, *125*. [[CrossRef](#)]
50. Ikuta, D.; Ohtani, E.; Fukui, H.; Sakamaki, T.; Heid, R.; Ishikawa, D.; Baron, A.Q.R. Density Deficit of Earth's Core Revealed by a Multimegabar Primary Pressure Scale. *Sci. Adv.* **2023**, *9*, eadh8706. [[CrossRef](#)] [[PubMed](#)]
51. Yoo, C.S.; Holmes, N.C.; Ross, M.; Webb, D.J.; Pike, C. Shock Temperatures and Melting of Iron at Earth Core Conditions. *Phys. Rev. Lett.* **1993**, *70*, 3931–3934. [[CrossRef](#)] [[PubMed](#)]
52. González-Cataldo, F.; Godwal, B.K.; Driver, K.; Jeanloz, R.; Militzer, B. Model of Ramp Compression of Diamond from Ab Initio Simulations. *Phys. Rev. B* **2021**, *104*, 134104. [[CrossRef](#)]
53. Swift, D.C.; Heuzé, O.; Lazicki, A.; Hamel, S.; Benedict, L.X.; Smith, R.F.; McNaney, J.M.; Ackland, G.J. Equation of State and Strength of Diamond in High-Pressure Ramp Loading. *Phys. Rev. B* **2022**, *105*, 014109. [[CrossRef](#)]
54. Sio, H.; Krygier, A.; Braun, D.G.; Rudd, R.E.; Bonev, S.A.; Coppari, F.; Millot, M.; Fratanduono, D.E.; Bhandarkar, N.; Bitter, M.; et al. Extended X-ray Absorption Fine Structure of Dynamically-Compressed Copper up to 1 Terapascal. *Nat. Commun.* **2023**, *14*, 7046. [[CrossRef](#)] [[PubMed](#)]

Disclaimer/Publisher's Note: The statements, opinions and data contained in all publications are solely those of the individual author(s) and contributor(s) and not of MDPI and/or the editor(s). MDPI and/or the editor(s) disclaim responsibility for any injury to people or property resulting from any ideas, methods, instructions or products referred to in the content.